Check for updates

Automated analysis of X-ray topography of 4H-SiC wafers: Image analysis, numerical computations, and artificial intelligence approaches for locating and characterizing screw dislocations

Binh Duong Nguyen[1,a)] , **Melissa Roder[2], Andreas Danilewsky[2], Johannes Steiner[3], Peter Wellmann[3], Stefan Sandfeld[1,4]**

[1] *Institute for Advanced Simulations – Materials Data Science and Informatics (IAS-9), Forschungszentrum Jülich GmbH, 52425 Jülich, Germany*
[2] *Kristallographie, Albert-Ludwigs-Universität Freiburg, 79104 Freiburg, Germany*
[3] *Crystal Growth Lab, Materials Department 6, Friedrich-Alexander University Erlangen-Nuremberg, 91058 Erlangen, Germany*
[4] *Chair of Materials Data Science and Materials Informatics, Faculty 5 – Georesources and Materials Engineering, RWTH Aachen University, 52056 Aachen, Germany*

a) Address all correspondence to this author. e-mail: bi.nguyen@fz-juelich.de

The physical vapor transport (PVT) crystal growth process of 4H-SiC wafers is typically accompanied by the occurrence of a large variety of defect types such as screw or edge dislocations, and basal plane dislocations. In particular, screw dislocations may have a strong negative influence on the performance of electronic devices due to the large, distorted or even hollow core of such dislocations. Therefore, analyzing and understanding these types of defects is crucial also for the production of high-quality semiconductor materials. This work uses automated image analysis to provide dislocation information for computing the stresses and strain energy of the wafer. Together with using a genetic algorithm this allows us to predict the dislocation positions, the Burgers vector magnitudes, and the most likely configuration of Burgers vector signs for the dislocations in the wafer.

Introduction

Understanding and controlling defects and their behavior is an essential task in semiconductor research and production, reducing the negative influence on electronic devices [1]. Furthermore, the predictive quality of simulations strongly depends on well-characterized defect structures, e.g., as initial values [2–6]. Many approaches have been performed to observe defects (e.g., micropipes (MPs) which are screw dislocations (SDs) with Burgers vector magnitude $b \geq 3c$, threading screw dislocations (TSDs)) in these materials. Transmission electron microscopy (TEM) [7] or high-resolution TEM [8] are applied for determining defect structure of GaN. Various groups used monochromatic or whitebeam synchrotron X-ray topography (SWXRT) in the Bragg geometry (back-reflection and grazing incidence, respectively) [9–13] for revealing and analyzing dislocation structures in SiC. Etching is another method for detecting dislocations in molten KOH [11, 14, 15].

The line direction of a SD (i.e., whether it is right-handed or left-handed) is given by the direction of the Burgers vector and is important for nucleation and interaction of defects. Its determination is at least difficult, and for complex dislocation arrangements nearly impossible. Generally, the determination of the line direction of SDs may be possible with TEM [16] but it is destructive, complicated, and locally limited to nm dimensions. Lang and Makepeace [17] analyzed Burgers vector directions (and thus indirectly the handedness of SDs) by synchrotron X-ray reticulography to map misorientations in a single crystal. This, however, can only be used to determine Burgers vectors larger than $\approx 8c$, with c the respective lattice parameter. By applying ray tracing simulation, Chen [18] introduced a non-destructive method to reveal the rotational direction of MPs and TSDs [19] in SiC by using grazing-incidence X-ray topography that employs *hkil*— and 0008—reflections, in which TSDs and MPs appear as white spots. Elliptical features, which are tilted

1254

clockwise from the orientation of the diffraction vector *g* represent left-handed MPs, those which are tilted counterclockwise are right-handed MPs. The line direction of a SDs becomes visible in the dark contrast enhancement side on the image, which is on the left for right-handed TSDs and on the right for left-handed TSDs. This, however, can only be used on perfectly contrasted regions and high-resolution topography images.

In this work, we present a different approach for extracting the position, magnitude, and sign of thousands of SDs from topography images using an automated image processing approach in combination. The application of an artificial intelligence approach (a genetic algorithm) allows to identify statistically likely configurations of Burgers vector directions such that the total internal energy is minimized. Together with a comparison to artificial dislocation structures, we can then conclude how far from an energy minimum the dislocation configuration of the crystal is. This elucidates the amount of eigenstress resulting from the growth process and thereby is an alternative property to quantify the microstructural defect state of a crystal.

Results and discussion

Analysis of dislocation positions and Burgers vector magnitude

For automated stitching of the more than 600 images, each of which was 575×382 pixels in size, an openCV-based code [20] was written. The resulting wafer image is shown in Fig. 1(a) and has 8624×8880 pixels. As only SDs are considered, a first image filter is defined that only leaves those white spots for which the area is approximately equal to that of an $1c$ up to $8c$ screw dislocation. The lower and upper limit for the area (i.e., the number of pixel) was obtained from the relation given in [13] which is visualized in Fig. 1(d).

A second filter then considers the shape of the white spots and eliminates all "non-SD spots" (e.g. those with long thin shaped contrasts). In order to do that, a possibly rotated ellipse was fitted to each white pixel cluster using a least-square strategy from openCV. Then, the ratio between major and minor ellipse axis, c_1 (governing the "lengthiness" of the pattern) could be obtained as well as the ratio between those pixel that are inside
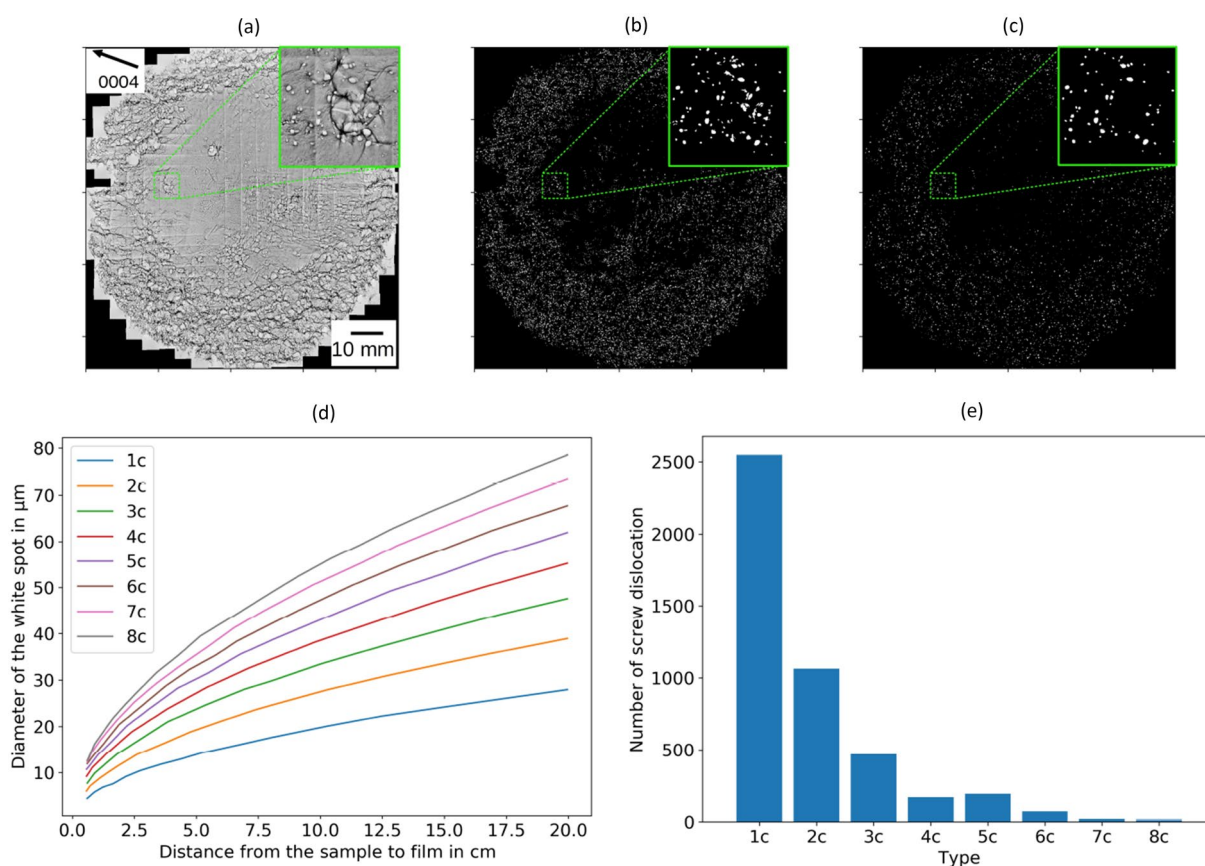
Figure 1: Postprocessing and analysis of X-ray back-reflection topography images (4H-SiC, 0004 - reflections): (a) stitched image (8624×8880 pixels); (b) applying a first filter leaves only areas corresponding to SDs type $1c$ ... $8c$; (c) applying filter 2 ensures correct SD shape; (d) relation between magnitude of Burger's vector, the diameter of the white spot and the distance from sample to film [13]; (e) resulting histogram of screw dislocation types observed (with $b \geq 3c$: SDs of MP-type).

the ellipse and the total ellipse area, c_2 (i.e., the "compactness" of the pixel cluster). Additionally, we also calculated the circularity of the white spots, defined as $c_3 = 4\pi A_{cont}/P_{cont}^2$, where A_{cont} and P_{cont} are the area and the perimeter of the white spot. For an ideal circular shape, c_3 would be 1. A detailed visual inspection of about 100 representative white spots showed that using the filter conditions of $c_1 \geq 3$, $c_2 \geq 0.65$, and $c_3 \geq 0.6$ is a robust approach to exclude all "non-SD spots." The resulting micrograph is shown in Fig. 1(c).

Figure 2 visualizes data of all extracted white spots from the topography image with respect to the three morphology parameters: lengthiness c_1, compactness c_2 , and circularity c_3.

From the dataset, we choose four specific points which are marked as red cross sign together with character A, B, C, and D. A($c_1 = 1.0$, $c_2 = 0.92$, $c_3 = 0.93$), and B($c_1 = 1.89$, $c_2 = 0.80$, $c_3 = 0.67$) are inside while C($c_1 = 4.96$, $c_2 = 0.64$, $c_3 = 0.25$), and D($c_1 = 2.20$, $c_2 = 0.57$, $c_3 = 0.31$) are outside of the filter region. The visualization of these specific positions are shown in first column of Fig. 3, respectively. The second and third columns of Fig. 3 illustrate the fitting ellipse to the white pixel cluster (2nd column) and pixel that are inside the ellipse (3rd column).

In a final step, these remaining bright spots can be classified as $1c$ to $8c$ screw dislocations according to the spots' diameters [13]. This results in the histogram shown in Fig. 1(e) and agrees well with manual counting within an small sub-area. The total number of screw dislocations is 4548, in which the $1c$-type occurs most often while the $7c$ and $8c$-type is only rarely seen.

Averaging the number of dislocation along the tangential direction of the disks results in dislocation density as a function of the radial direction distance from the center. These are plotted

Figure 2: Shown are all extracted white spots as a function of the three parameters: lengthiness c_1, compactness c_2 , and circularity c_3.

for each dislocation type in Fig. 4(a), where the average density of the $1c$-type is $3.08 \cdot 10^5$ cm^{-2} and the average density of the $8c$-type is $1.09 \cdot 10^4$ cm^{-2}. Figure 4(b) shows the density of total dislocation types together with the density of two artificial configurations, where the number of dislocations is chosen equal to the real configuration. For visualization purpose, Figs. 4(c) and (d) are drawn with lower number of dislocations, with a total number of 463 SDs for both configurations.

An important but so far missing information that is needed to fully characterize the dislocations in the wafer are the signs of the Burgers vectors and/or the line directions: they define whether a screw dislocation is termed a right-handed screw (RHS) or a left-handed screw (LHS) dislocation. For example, RHS is tantamount with a plastic deformation in the direction of the Burgers vector while a LHS comes with plastic deformation in the opposite direction. As a consequence, the displacement and strain field for a RHS with $+\mathbf{b}$ are the same as the one resulting from a LHS with $-\mathbf{b}$. The following analyses investigate the influence of the screw dislocation position and handedness on the internal energy and asks, what the most probable configuration might be.

Often, threading dislocations with predominant screw components are—in commercial SiC—actually threading mixed dislocations with Burgers vector $nc + ma$ (n and m integers) [21]. However, as a first approximation, we only consider the predominant screw component and assume that those white spots are all SDs.

Also, the wafer offcut does not influence our X-ray and optical characterization methods and the analysis. It is important to know for an easier and faster orientation to fix the wished diffraction vector. In general, a special value of offcut is chosen for further use as a seed and for epitaxial growth because it influences the growth modes. The step flow direction and macrostep formation may affect the growth defects (like it is known, e.g., from liquid phase epitaxy of III–V-compounds). We see some preferred defect directions, which may be the result of this. But actually, we do not have enough data to explain a defined correlation. This may be the subject of further experiments.

Analysis of dislocation configurations in terms of strain energy density

As a baseline for the analysis of the experimental topographs, Fig. 1, we create artificial dislocation distributions that cover two extreme cases in terms of internal strain energy density: the first is a homogeneous SD distribution with constant dislocation density that has a low internal energy, while the second one has a very pronounced, logarithmic dislocation gradient along the radial direction and therefore results in high internal stresses and strains, see Fig. 4. These structures elucidate the correlation between the wafer-dislocation structure and
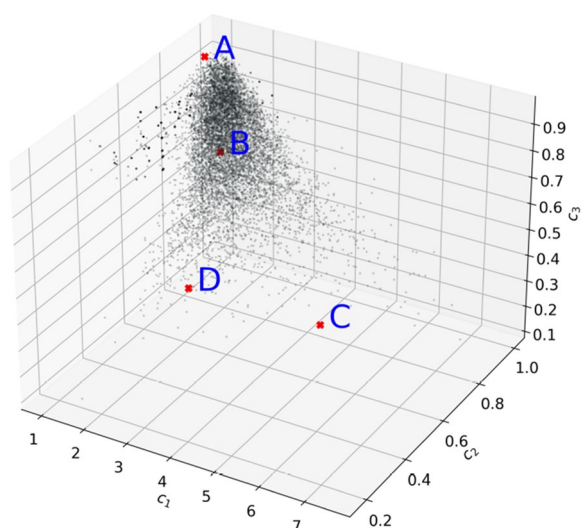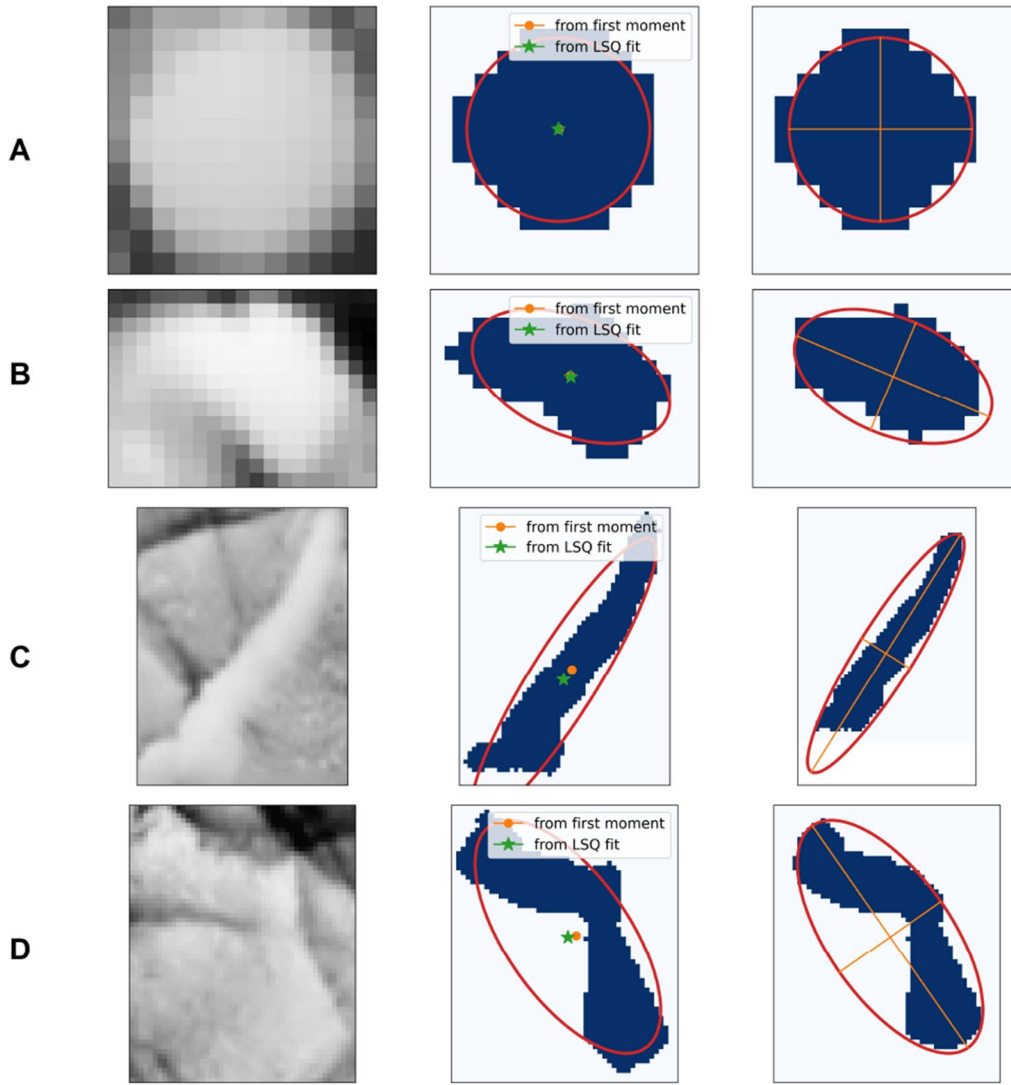
Figure 3: Examples of data at specific points A, B, C, and D.
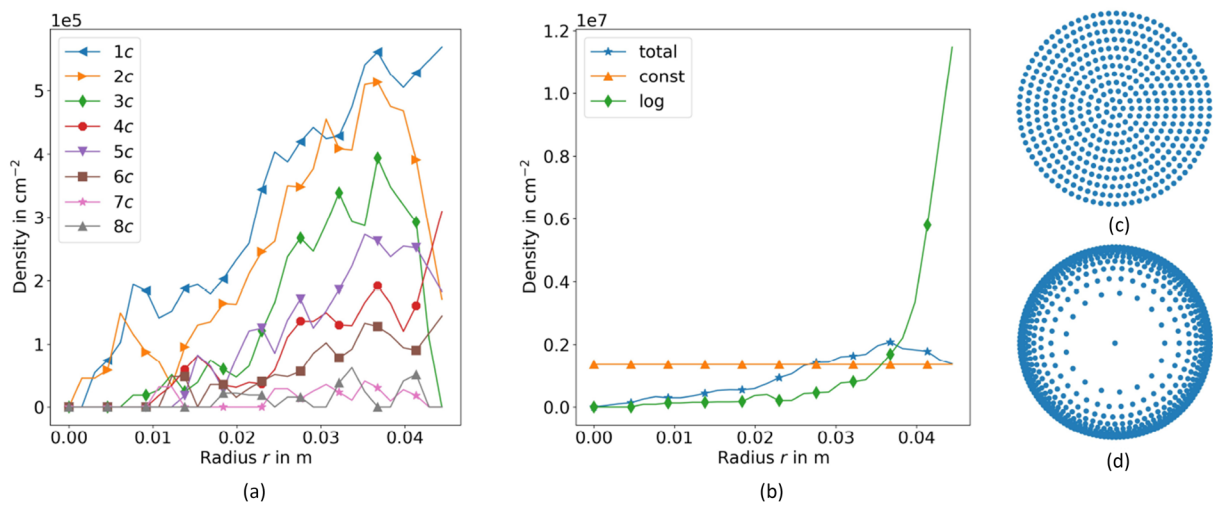
Figure 4: Dislocation density along the radial axis: (a) from 1c to 8c of real configuration; (b) total density of real configuration and density from two exemplary distributions of screw dislocations in 2D with (c) constant spacing; (d) logarithmic spacing.

the resulting energy distribution and help to classify the real dislocation structure with respect to the two extreme cases.

Here, we simplify for radial symmetry, but in reality we would expect and really see the assymmetry by the off-orientation and gradients.

In the following, these artificial configurations are analyzed for 4H-SiC single crystal material with shear modulus $G = 193\,\text{GPa}$, wafer radius $R = 5\,\text{cm}$, Burgers vector magnitude $b = 1c$ with c the length of the hexagonal unit cell along the c-axis ($c = 1\,\text{nm}$ for 4H-SiC according to [22]). The dislocation line is perpendicular to the wafer surface and in z-direction.

Two different configurations in terms of the Burgers vectors (or line directions, respectively) are investigated: (i) only right-handed SDs (left-handed SDs result in stresses multiplied by -1 and in the same energy density), and (ii) a random distribution of both signs. The resulting stress and energy density are shown in the first two rows of the two image groups in Fig. 5 for stress and energy density. There, the "dark spots" in the stress fields are a result of the diverging stress values directly at the dislocation core; while they indicate the positions of the dislocations they are not manually added "markers." For larger numbers of dislocations this makes the plots of the artificial structures difficult to read. Therefore, for the artificial systems, we reduced the number of dislocations but scaled the Burgers vector such that these dislocation distributions have the same Burgers vector content as the topography image. The Burgers vector content is calculated by taking average of the magnitude of Burgers vector ($1c$ to $8c$) from real configuration as $\langle b \rangle \approx b_{\text{tot}}/n_{\text{disloc}} = 1.85c$, where total of Burgers vector magnitude, $b_{\text{tot}} = \sum_{n=1}^{n_{\text{disloc}}} b_n = 8400c$, and number of screw dislocations, $n_{\text{disloc}} = 4548$. The following aspects can be observed in Fig. 5:

1. Homogeneous dislocation distribution—first column of Fig. 5:

   • One observes low values of average stress [Fig. 5(a)] and energy density [Fig. 5(d)] if the signs of the Burgers vectors are the same. There, shear stresses τ_{xz} partially cancel out between vertically aligned dislocations due to the symmetry $\tau_{xy}(x, y) = -\tau_{xy}(x, -y)$ in equation (1). The gradient of the stress distribution in vertical direction is due to the distribution of dislocations in the circular domain causing a deviation from the regular dislocation arrangement.

   • When the signs of the SDs in the homogeneous distribution are chosen randomly, patches of high stresses occur when nearby dislocations along the y direction have opposite signs, and to a lesser degree also when dislocations with the same sign are

located horizontally, Fig. 5(b). The energy density, Fig. 5(e), follows this pattern but is also determined by the other non-zero shear stress component.

2. Dislocation density increases toward the edge of the wafer—second column of Fig. 5:

   • Stresses add up in vertical direction similar to a dislocation pile-up which leads to the high values of stress distribution [Fig. 5(g)] as well as to a significantly higher energy density distribution as compared to the homogeneous distribution, Fig. 5(j). This is due to the fact that a dislocation pile-up stores a large amount of elastic energy.

   • For the logarithmic spacing, the energy density distribution depends very strongly on the degree of randomness of the line direction signs: dislocations with alternating line directions in radial direction "break up" the pileups and thereby strongly lower the stored energy as can be seen when comparing Figs. 5(h) and (i).

3. Dislocation position according to topography analysis: third column of Fig. 5:

   • Given the dislocation position as extracted from the topography and choosing the handedness for all dislocations results in Fig. 5(m) in a stress distribution that, except for a rotation and offset, is comparable to that found for the logarithmic spacing: the whole wafer is separated by a line into a region of positive and negative stress. This clearly shows that the increasing density toward the surface is the predominant feature of the wafer.

   • When the line sense is chosen randomly, stress values are strongly reduced and distributed more equally throughout the domain [Fig. 5(n)]. The energy density level, Fig. 5(q) is also strongly reduced, but on average is higher than that of the first two dislocation configurations. This is due to the particular type of distribution that, in the wafer encompasses a larger region than in the "logarithmic distribution."

Identifying likely and unlikely Burgers vector configurations using a genetic algorithm (GA)

We now analyze the energy of the wafer of the actual dislocation configuration from the topography data, i.e., dislocation positions as in the right column of Fig. 5. Two types of studies are performed: (i) determining the Burgers vector signs using a genetic algorithm (GA) such that a low-energy state is achieved (cf. Eq. (5)) and (ii) using a GA to minimize the energy as a function of the dislocation positions for given Burgers vector signs.
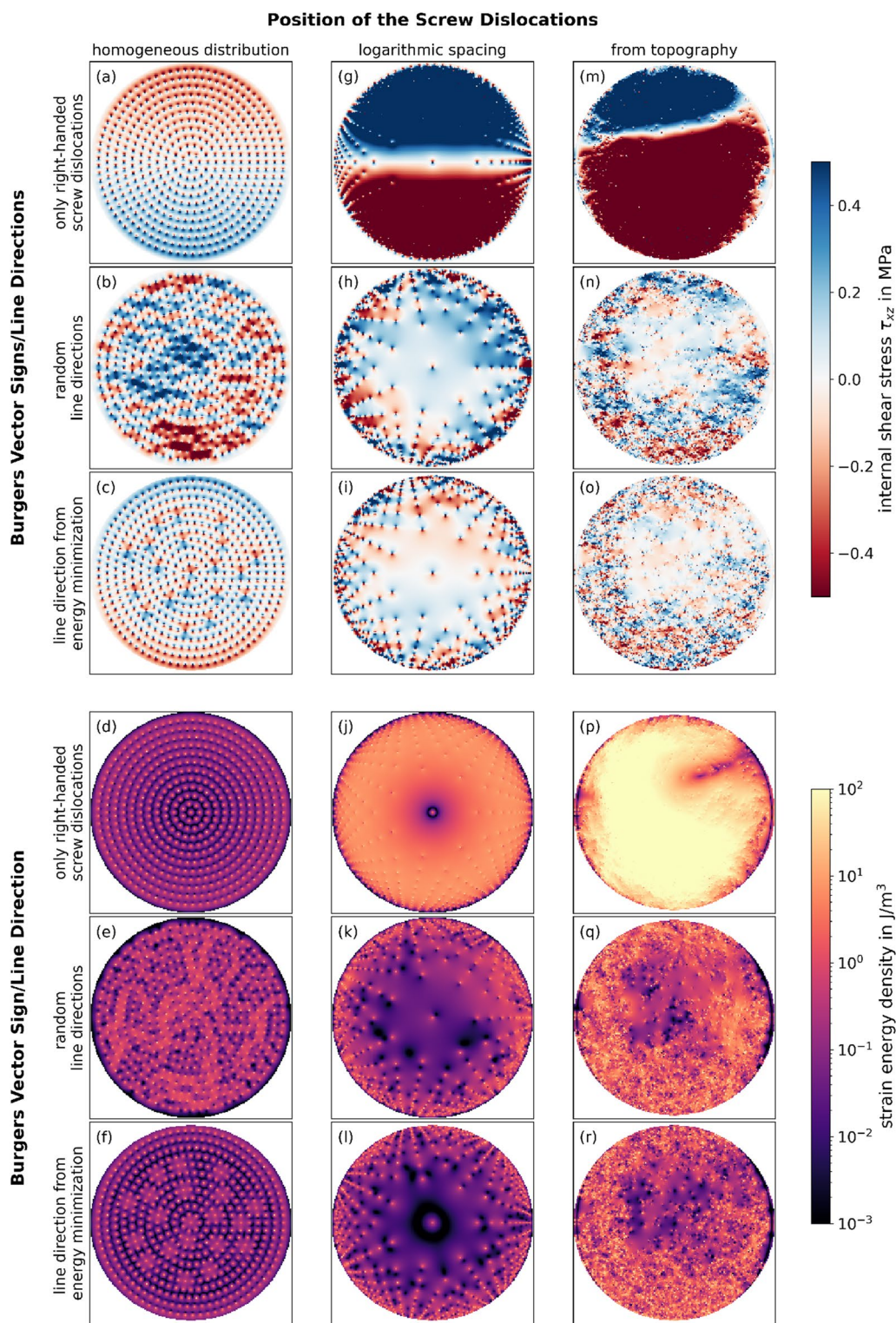
Figure 5: Shear stress τ_{xz} (top half) and strain energy density ψ (bottom half) of two artificial and a real dislocation distribution (plots in columns) for three different Burgers vector sign constellations (in the rows of the top and bottom half). The Burgers vectors of the two artificial systems (column 1 and 2) are scaled such that the effective Burgers vector content is the same as in the real dataset shown in the third column.

A GA as a classical artificial intelligence method is inspired by the evolution of nature, performs a heuristic search process, and thereby is able to learn. By relying on operations such as mutation, crossover, and selection, the algorithm finds the fittest individuals from the predefined population to produce the offspring for the next generation. For a general introduction to the concept of GA please refer to, e.g., [23].

For finding the lowest possible energy state with a GA the open source python framework DEAP [24] was used. There, the "individuals" are the dislocations' positions and/or Burgers vector signs, and the algorithm is able to learn, e.g., which configurations result in higher energy states. The GA "simulations" were run with 400 populations in 1000 generations. The probability for mutation and crossover in each generation is chosen to be 0.2 and 0.5, respectively. At the beginning of the first type of energy minimization, there are 400 populations of randomly generated individuals, i.e., Burger's vector signs. The algorithm then evaluates the objective function of the optimization problem, i.e., the energy, for each individual of the population. The "fittest individuals" are chosen from the current population, and they can be recombined or mutated based on the probability to form a new generation for the next iteration. The algorithm stops when the energy does not change appreciably anymore which was the case after roughly 1000 generations.

The resulting total strain energies per unit length are summarized in Fig. 6 for all 15 combinations of spatial dislocation configurations [the columns of Fig. 6(a)] and for all Burgers vectors sign configurations [the rows of Fig. 6(a)]. The respective distributions (labeled with capital letters (A)–(L)) are shown in Fig. 6(b), giving an idea about the scatter of the data. An additional asterisk indicates that the data are obtained from GA, and shown is the median of 10 such computation. All other data are obtained as the median of 1000 statistically equivalent calculation. The following can be summarized for the data of the first four columns:

1. If dislocations are distributed homogeneously and · · ·

   - · · · either have the same line direction [Fig. 5(d)] or have line directions obtained from energy minimization [Fig. 5(f)] then the total energy is about the same with a value of 77 and 73 J/m, respectively.
   - · · · have random line directions [Fig. 5(e)] the total energy is by 30% higher with a value of 100 J/m.

2. If dislocations are distributed with logarithmic spacing ...

   - · · · then the dependence of the total energy on the Burgers vector is quite extreme with a high value of 3136 J/m for logarithmic spacing with RHS dislocations [Fig. 5(j)] ...
   - · · · and very similar values of 55 J/m and 41 J/m for the other two cases [Fig. 5(k) and (l)].

3. For the real dislocation positions obtained from topography · · ·

   - · · · the total energy follows the same trend and has a very high value if all dislocations would have the same line direction (1782 J/m), Fig. 5(p)
   - · · · while the energy for the minimized configuration gives a low value 80 J/m and a higher value of 101 J/m for the random configuration, Fig. 5(r) and (q).
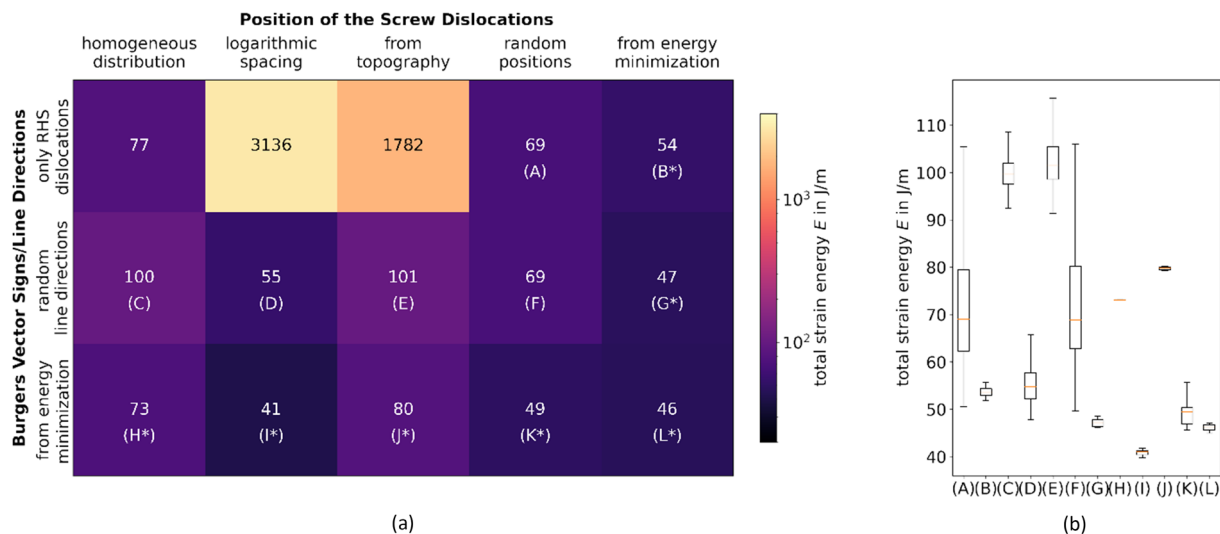
Figure 6: (a) Total strain energies for all studied combinations of dislocation positions and line directions. (b) Box plot for each random case which are labeled in (a).

4. If dislocations are at random positions then the total energies are almost the same with a value of 69 J/m for the cases of random line direction and RHS dislocations, while it is 49 J/m for line directions obtained from energy minimization.

We now examine the simulation with the same number of dislocations (4548) and Burgers vector magnitude ($1c$–$8c$) for which the position of dislocations will be automatically arranged by the minimization process (right column of Fig. 6). Clearly, such a "particle model" is strongly idealized; it violates the fact that dislocations move on slip planes and might form quasi-stable jammed configurations. However, this model can serve as a baseline and estimate, such that we can observe the correspondence between microstructure and energy state of the wafer.

Burgers vector signs are randomly chosen, and the same GA set up as above is used to find those dislocation positions that minimize the wafer's energy. Figure 7(a)–(d) shows the best solution at the very 1st generation and at the 1000th generation [Fig. 7(e)–(h)]. We observe that, in general, dislocations spread out evenly within the whole domain, although Fig. 7(e) exhibits a some local clustering of dislocation.

In comparison to Fig. 5 the stresses are after 1000 generations rather equally distributed, except for a few banded structures.

This is even more pronounced in the energy density shown in Fig. 7(h). The corresponding energy has a value of around 47 J/m (see Fig. 6). Computation for this case using as the Burger

vectors only right-handed dislocations gives a total energy of 54 J/m, while from energy minimization we obtain—on average—a total energy of 46 J/m. The energy from this minimization shows that the state where the real wafer is at the moment may not be the minimum state of energy. This is plausible as in reality, the energy of the wafer also will depend on other types of defects and therefore might not be at a lowest energy state.

We see that the lowest energy (41 J/m) results from the (unrealistic) logarithmic spacing and the minimization process with respect to line directions, whereas the highest energy (3136 J/m) results from the (unrealistic) logarithmic spacing with only right-hand side dislocations.

The distribution of data in Fig. 6(b) shows that the minimization process works very well for finding the global minimum (indicated by the small variance of the data) while the randomness obviously results in wider range of the values.

Assuming only RHS dislocations results in very different energy values for different spatial dislocations configurations. In particular, the logarithmic positioning and the real positions from topography result in extremely high values. The lowest values are, for a specific spatial configuration, always obtained when the Burgers vector direction is obtained from the energy minimization. There, it seems that the value of ≈ 41 J/m is a lower limit. In terms of energy values, the real configuration with an average value of 80 J/m is closest to the homogeneous distribution with the Burgers vector sign determined by energy minimization. As these two situations
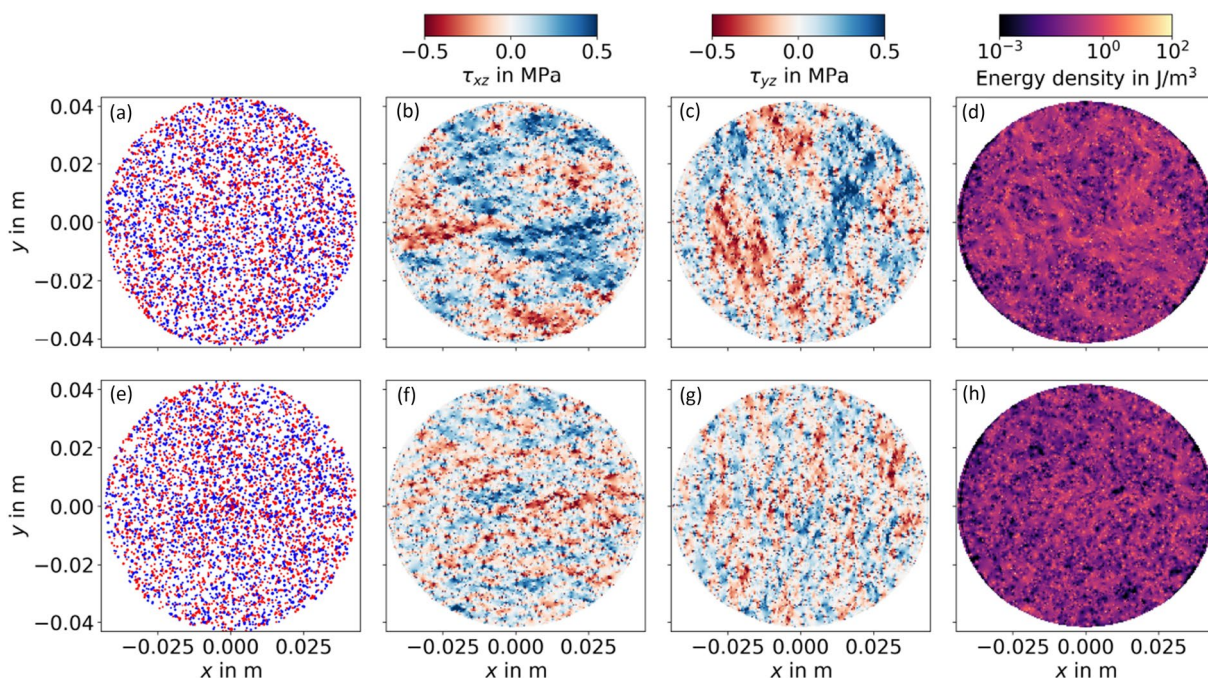
Figure 7: Wafer state: at 1st generation (a)–(d) and at 1000th generation (e, f) (from left to right): (a) and (e) dislocation positions (blue/red dots: positive/negative Burgers vectors); (b) and (f), (c) and (g) shear stresses distribution; (d) and (h) energy density distribution. The total strain energies are 73 and 46 J/m, respectively.

again have nearly the same energy values also for random line directions we conclude that the real configuration is more similar to a homogeneous distribution than a distribution with a pronounced dislocation density gradient toward the surface as the logarithmic spacing, a random positioning, or a distribution from minimization process.

Assuming that the most likely distribution of Burgers vector sign is such that it minimizes the energy of the wafer for fixed dislocation positions, our simulation shows that a random distribution is already quite close to such a configuration.

However, it needs to be pointed out that such a "energy minimization argument" should only be understood as a first approximation as dislocations are not free to arbitrarily flip the line direction, e.g., during the growth process.

Clearly, our study is based on an idealized model as in real crystals there often also other types defects present, to start with. Furthermore, the dislocation structure might not be arranged such that the energy is at a minimum: the location of defects may be determined by details of the growth seed therefore might be fixed during the subsequent growth process, resulting in additional eigenstrain.

Additionally, the distribution that we actually see in the topography is a *post mortem* structure at room temperature which is frozen during the cooling, i.e., the transition from ductile to brittle. This significantly reduces the dislocation mobility such that dislocations might "get stuck" in an energy state far from a global energy minimum. All of this also creates a strong history dependence of the real dislocation structure that can not be "guessed" or inversely modeled from a single microscopy snapshot in time.

In how far are the above computational studies reliable and useful for understanding the *real* dislocation state? Assuming that the extracted number and type of dislocation using our automated image analysis is reliable, we are now in the situation where we understand how different arrangements of dislocations and their Burgers vector signs give rise to different stress and energy states—including the consideration of image forces at the surfaces (edge of the wafer). The so obtained total energy values shown in Fig. 6 determine the range within which the true energy can be assumed: most probably the true Burgers vector signs are such that they exhibit "energy minimizing aspects" but also show some randomness, which suggests a value in the range of $\approx$ 80–101 J/m.

The presented study provides analysis concepts and tools to evaluate further and improve the SiC bulk growth process. (i) The automated analysis of the X-ray topography measurements enables a precise determination of the distribution of SDs, including the size of the Burgers vector. The latter knowledge, i.e., the Burgers vector exhibiting values of $b = 1c \ldots 8c$ (with $b \geq 3c$: SDs of MP-type), sheds light on the formation mechanism of the SDs during growth or the

subsequent cooling down. In particular, Burgers vectors of $c \geq 2c$ imply distortions of the growth process due to particle inclusions (e.g. carbon dust), voids, or unintentional polytype instabilities.

The developed image analysis of the X-ray topography provides a valuable tool for studying the SiC growth process. (ii) The numerical calculation of the total line energy of the distributions of the SDs, including a proposition of the Burger's vector direction, allows a comparison of the real crystal's condition after growth compared with a theoretical optimum case of minimum energy. This way, the deviation of the total energy between real and optimum value may be used to optimize the cooling down process after the growth process and a post-growth annealing procedure of the SiC boule. In many cases of SiC bulk growth by the PVT method, the SiC boule will be cooled down in a non-isothermal temperature field. After passing the transition from the ductile to brittle at around 1150 °C, this leads to a freezing of the dislocation distribution, which is one source for the deviation of the real dislocation state from a minimum energy one. The presented work may be applied to quantify this deviation.

Another relevant source for the deviation of the real dislocation state from a minimum energy one, which cannot yet be distinguished within our model, is a too fast or too slow cooling down ramp. In the first case, desired dislocation glide will remain incomplete. In the second case, dislocation multiplication will cause an increase in the dislocation density. In order to elucidate such a phenomenon, implementing the actual strain field and dislocation glide, dislocation generation, and annihilation would need to be considered in a more global approach.

Nevertheless, the already achieved estimation of the total SD line energy for various dislocation configurations indicates that this work can be further extended by including threading edge and basal plane dislocations. The experimental determination of the density and distribution of threading edge dislocations (TEDs) and basal plane dislocations (BPDs) by X-ray topography is more complicated than in the case of SDs. However, the above-presented modeling approach using energy minimization of a virtual dislocation state proves to be quite powerful to predict SD dislocation distribution. Hence, a transfer of the model to calculate configurations of TEDs and BPDs in order to predict their occurrence in real crystals should be possible.

Conclusions

We have analyzed 2D distributions of dislocations in a wafer, based on digital X-ray topography images and artificial situations, to understand the dislocations' effect on the energy of the system. Using a Genetic Algorithm, we have predicted the Burgers vector signs in the wafer assuming that they are such as to minimize the energy.

In order to find a more realistic Burgers vector sign distribution one will need to investigate the whole three-dimensional structure including the growth process, which currently is still a nearly impossible difficult task. But already the comparison of the energy in this 2D setting gives a general overview of the lower and upper limit of the resulting energies from screw dislocations.

This helped to understand which are likely Burgers vector sign configurations and thereby to estimate the energy that is not directly accessible from the topography images. Altogether, the developed analysis framework will be a valuable tool fo the crystal growth community to obtain information about the energetic state of the dislocation microstructure and to tailor the growth and cooling down process parameters. Ultimately, this will help to create crystals with a strongly reduced defect density and thereby to create electronic devices with enhanced properties.

Microscopy, theory, and methods

Topography images

The topography images were obtained from SWXRT mapping of a 100 mm 4H-SiC (0001) wafer cut with an off-orientation of $\approx 4°$. The analysis of the full wafer topography and the SiC wafer cut is described in detail in [25]. The SWXRT measurements were carried out at the imaging cluster of the Karlsruhe Institute of Technology light source "KARA" [26].

For the adjustment of the wafer in back-reflection geometry, the X-ray-sensitive film is placed between the sample and the slit system with a distance of about 80 mm to 100 mm, to collect the diffracted Laue pattern.

For a full wafer mapping, an indirect 2D digital dectector system is chosen to image the 0004 reflection. The high-resolution imaging systems includes a scintillator crystal, an optical macroscope, and the pco.4000 fast, high-resolution CCD camera with a resolution of 4008 × 2672 pixels per image.

The physical beam size for each topograph is 5 mm × 7 mm, and the mapping of the wafer was performed with equidistant step size in x and y direction. Due to a tilting and straining of the wafer, a geometrical distortion of the diffracted images resulted and thus, the camera position had to be corrected individually for each topograph.

When the X-rays diffract from the deformed region close to the dislocation core, it causes many tilted diffracted beams in various directions with a loss of intensity that is observed as the white and black spots on the topographs on X-ray film and CCD camera, respectively [13]. Note that for consistence of film and CCD images, all of the digital topographs shown in this paper are inverted. Depending on the size and contrast of the circular spots [10], dislocations can be identified either as MPs, TSDs, or TEDs. The shape of the white spots can also be elliptical because of too close neighboring TEDs/MPs or geometrical deformation as a result of the diffraction projection. MPs correspond to larger white spots and have stronger contrast than TSDs due to their wider strain field. TSDs are smaller than MPs but also have a strong contrast, i.e., a strong strain field. White spots from TEDs are much smaller than those from TSDs but generally are associated with a strain field of low magnitude, therefore lacking contrast.

In addition to MPs, SDs, and TEDs, further large, white pixel clusters of irregular shape are partially depicted on some reflections, which do not fit the description of any type of screw dislocation or edge dislocation. These features were identified as voids with the usage of polarization microscopy. TSDs and MPs show both screw character, with different magnitudes of Burgers vectors. Most of their dislocation lines are approximately parallel to the c-axis, and their Burgers vectors are parallel to the line. BPDs of mainly mixed character are also present and visible as fine black lines in the topographs. They are, however, in this first analysis within the current work neglected.

Computation of stresses and strain energy

Assuming that the position of the relevant dislocations in the wafer is known, the resulting stress, strain, and energy density fields for a complex microstructure can be obtained as linear superposition of the respective fields of single dislocations. Additionally, the free surfaces (edges of the wafer) need to be considered which give rise to image forces. For a right-handed SD piercing, a finite circular domain of radius R at (x_p, y_p) the non-zero stress tensor components can be obtained from the following equations [27]:

$$\tau_{xz}(x,y) = -\frac{Gb}{2\pi}\frac{y - y_p}{(x - x_p)^2 + (y - y_p)^2}$$
$$+ \frac{Gb}{2\pi}\frac{y - y_p R^2/(x_p^2 + y_p^2)}{(x - x_p R^2/(x_p^2 + y_p^2))^2 + (y - y_p R^2/(x_p^2 + y_p^2))^2}$$

$$(1)$$

$$\tau_{yz}(x,y) = +\frac{Gb}{2\pi}\frac{x - x_p}{(x - x_p)^2 + (y - y_p)^2}$$
$$- \frac{Gb}{2\pi}\frac{x - x_p R^2/(x_p^2 + y_p^2)}{(x - x_p R^2/(x_p^2 + y_p^2))^2 + (y - y_p R^2/(x_p^2 + y_p^2))^2},$$

$$(2)$$

The first term governs the stress field in an infinite domain, while the second term takes the effect of the dislocations images into account and is required to make the surfaces traction free. For left-handed SDs b is replaced by $-b$.

Assuming linear elasticity, the resulting stresses of the n SDs in the wafer are then obtained from linear superposition. The non-zero stress tensor components are

$$\tau_{xz}^{tot}(x,y) = \sum_{i=1}^{n}\tau_{xz}^{i}(x,y) \quad \text{and} \quad \tau_{yz}^{tot}(x,y) = \sum_{i=1}^{n}\tau_{yz}^{i}(x,y),$$

$$(3)$$

and the energy density ψ is given by

$$\psi(x,y) = \frac{1}{2G}\left(\left(\tau_{xz}^{\text{tot}}(x,y)\right)^2 + \left(\tau_{yz}^{\text{tot}}(x,y)\right)^2\right). \quad (4)$$

The total strain energy, E, is obtained by integrating the energy density over the wafer area,

$$E = \int_A \psi \, \mathrm{d}A = \frac{1}{2G}\int_A \left(\tau_{xz}^{\text{tot}}(x,y)\right)^2 \mathrm{d}A + \frac{1}{2G}\int_A \left(\tau_{yz}^{\text{tot}}(x,y)\right)^2 \mathrm{d}A. \quad (5)$$

Acknowledgments

Funding

Data availability

Data available upon request.

Code availability

Code available upon request.

Declarations

Conflict of interest: On behalf of all authors, the corresponding author states that there is no conflict of interest.

Open Access

References

1. S. Mahajan, Defects in semiconductors and their effects on devices. Acta Mater. **48**(1), 137–149 (2000). https://doi.org/10.1016/S1359-6454(99)00292-X

2. T. Hochrainer, S. Sandfeld, M. Zaiser, P. Gumbsch, Continuum dislocation dynamics: towards a physical theory of crystal plasticity. J. Mech. Phys. Solids **63**, 167–178 (2014). https://doi.org/10.1016/j.jmps.2013.09.012

3. S. Sandfeld, M. Zaiser, Pattern formation in a minimal model of continuum dislocation plasticity. Modell. Simul. Mater. Sci. Eng. **23**(6), 065005 (2015). https://doi.org/10.1088/0965-0393/23/6/065005

4. S. Sandfeld, G. Po, Microstructural comparison of the kinematics of discrete and continuum dislocations models. Modell. Simul. Mater. Sci. Eng. **23**(8), 085003 (2015). https://doi.org/10.1088/0965-0393/23/8/085003

5. B.D. Nguyen, A.M. Rausch, J. Steiner, P. Wellmann, S. Sandfeld, On the importance of dislocation flow in continuum plasticity models for semiconductor materials. J. Cryst. Growth **532**, 125414 (2020). https://doi.org/10.1016/j.jcrysgro.2019.125414

6. Y. Cui, T. Wang, S. Luo, Z. Li, Z. Li, A discrete-continuous model of three-dimensional dislocation elastodynamics. Int. J. Plast. **152**, 103221 (2022). https://doi.org/10.1016/j.ijplas.2022.103221

7. T. Metzger, R. Höpler, E. Born, O. Ambacher, M. Stutzmann, R. Stömmer, M. Schuster, H. Göbel, S. Christiansen, M. Albrecht et al., Defect structure of epitaxial gan films determined by transmission electron microscopy and triple-axis x-ray diffractometry. Philos. Mag. A **77**(4), 1013–1025 (1998). https://doi.org/10.1080/01418619808221225

8. S. Li, J. Chen, P. Ruterana, The [10-10] edge dislocation in the wurtzite structure: a high-resolution transmission electron microscopy investigation of [0001] tilt grain boundaries in GaN and ZnO. Acta Mater. **175**, 457–465 (2019). https://doi.org/10.1016/j.actamat.2019.06.044

9. M. Dudley, S. Wang, W. Huang, C.H. Carter Jr., V. Tsvetkov, C. Fazi, White-beam synchrotron topographic studies of defects in 6H-SiC single crystals. J. Phys. D **28**(4A), 63 (1995). https://doi.org/10.1088/0022-3727/28/4a/012

10. X. Huang, M. Dudley, W. Vetter, W. Huang, W. Si, C. Carter Jr., Superscrew dislocation contrast on synchrotron white-beam topographs: an accurate description of the direct dislocation image. J. Appl. Crystallogr. **32**(3), 516–524 (1999). https://doi.org/10.1107/S0021889899002939

11. S. Sintonen, M. Rudziński, S. Suihkonen, H. Jussila, M. Knetzger, E. Meissner, A. Danilewsky, T.O. Tuomi, H. Lipsanen, Synchrotron radiation x-ray topography and defect selective etching analysis of threading dislocations in gan. J. Appl. Phys. **116**(8), 083504 (2014). https://doi.org/10.1063/1.4893901

12. Dhanaraj, G., Raghothamachar, B., Dudley, M.: Growth and characterization of silicon carbide crystals. In: Springer Handbook of Crystal Growth, pp. 797–820. Springer (2010). https://doi.org/10.1007/978-3-540-74761-1_23

13. Dudley, M., Huang, X.: Characterization of SiC using synchrotron white beam X-ray topography. In: Materials Science Forum, vol. 338, pp. 431–436. Trans Tech Publ (2000). https://doi.org/10.4028/www.scientific.net/MSF.338-342.431

14. Sakwe, S.A., Herro, Z., Wellmann, P.J.: Development of a KOH defect etching furnace with absolute in-situ temperature measurement capability. In: Materials Science Forum, vol. 483, pp. 283–286. Trans Tech Publ (2005). https://doi.org/10.4028/www.scientific.net/MSF.483-485.283

15. S. Mahajan, M. Rokade, S. Ali, K.S. Rao, N. Munirathnam, T. Prakash, D. Amalnerkar, Investigation of micropipe and defects in molten KOH etching of 6H n-silicon carbide (SiC) single crystal. Mater. Lett. **101**, 72–75 (2013). https://doi.org/10.1016/j.matlet.2013.03.079

16. G. Groves, M. Whelan, The determination of the sense of the burgers vector of a dislocation from its electron microscope images. Philos. Mag. **7**(81), 1603–1607 (1962). https://doi.org/10.1080/14786436208213295

17. A. Lang, A. Makepeace, Synchrotron x-ray reticulography: principles and applications. J. Phys. D **32**(10A), 97 (1999). https://doi.org/10.1088/0022-3727/32/10a/321

18. Chen, Y., Huang, X.R., Dhanaraj, G., Dudley, M., Sanchez, E., MacMillan, M.F.: Sense determination of c-axis screw dislocations in 4H-SiC. In: Materials Science Forum, vol. 600, pp. 297–300. Trans Tech Publ (2009). https://doi.org/10.4028/www.scientific.net/MSF.600-603.297

19. Y. Chen, M. Dudley, Direct determination of dislocation sense of closed-core threading screw dislocations using synchrotron white beam x-ray topography in 4H silicon carbide. Appl. Phys. Lett. **91**(14), 141918 (2007). https://doi.org/10.1063/1.2793705

20. Bradski, G.: The OpenCV Library. Dr. Dobb's Journal of Software Tools (2000)

21. Guo, J.Q., Yang, Y., Wu, F.Z., Sumakeris, J.J., Leonard, R., Goue, O., Raghothamachar, B., Dudley, M.: Using ray tracing simulations for direct determination of burgers vectors of threading mixed dislocations in 4h-sic c-plane wafers grown by pvt method. In: Materials Science Forum, vol. 858, pp. 15–18. Trans Tech Publ (2016). https://doi.org/10.4028/www.scientific.net/MSF.858.15

22. Maximenko, S.I., Pirouz, P., Sudarshan, T.S.: Open core dislocations and surface energy of SiC. In: Materials Science Forum, vol. 527, pp. 439–442. Trans Tech Publ (2006). https://doi.org/10.4028/www.scientific.net/MSF.527-529.439

23. J.H. Holland, Genetic algorithms. Sci. Am. **267**(1), 66–73 (1992)

24. F.-A. Fortin, F.-M. De Rainville, M.-A. Gardner, M. Parizeau, C. Gagné, DEAP: evolutionary algorithms made easy. J. Mach. Learn. Res. **13**, 2171–2175 (2012)

25. J. Steiner, M. Roder, B.D. Nguyen, S. Sandfeld, A. Danilewsky, P.J. Wellmann, Analysis of the basal plane dislocation density and thermomechanical stress during 100 mm PVT growth of 4H-SiC. Materials **12**(13), 2207 (2019). https://doi.org/10.3390/ma12132207

26. A. Rack, T. Weitkamp, S.B. Trabelsi, P. Modregger, A. Cecilia, T. dos Santos Rolo, T. Rack, D. Haas, R. Simon, R. Heldele, M. Schulz, B. Mayzel, A.N. Danilewsky, T. Waterstradt, W. Diete, H. Riesemeier, B.R. Mueller, T. Baumbach, The micro-imaging station of the topotomo beamline at the anka synchrotron light source. Nucl. Instrum. Methods Phys. Res. B **267**(11), 1978–1988 (2009). https://doi.org/10.1016/j.nimb.2009.04.002

27. C.R. Weinberger, The structure and energetics of, and the plasticity caused by, eshelby dislocations. Int. J. Plast. **27**(9), 1391–1408 (2011). https://doi.org/10.1016/j.ijplas.2011.03.004